ACS NANO

www.acsnano.org

ARTICLE

Directional Radiative Cooling via Exceptional Epsilon-Based Microcavities

Jin-Woo Cho, Yun-Jo Lee, Jae-Hyun Kim, Run Hu,* Eungkyu Lee,* and Sun-Kyung Kim*

Cite This: *ACS Nano* 2023, 17, 10442−10451

Read Online

ACCESS | Metrics & More | Article Recommendations | Supporting Information

ABSTRACT: The advent of nanophotonics enables the regulation of thermal emission in the momentum domain as well as in the frequency domain. However, earlier attempts to steer thermal emission in a certain direction were restricted to a narrow spectrum or specific polarization, and thus their average (8−14 μm) emissivity (ε_{av}) and angular selectivity were nominal. Therefore, the practical uses of directional thermal emitters have remained unclarified. Here, we report broadband, polarization-irrelevant, amplified directional thermal emission from hollow microcavities covered with deep-subwavelength-thickness oxide shells. A hexagonal array of SiO_2/AlO_X (100/100 nm) hollow microcavities designed by Bayesian optimization exhibited ε_{av} values of 0.51−0.62 at 60°−75° and 0.29−0.32 at 5°−20°, yielding a parabolic antenna-shaped distribution. The angular selectivity peaked at 8, 9.1, 10.9, and 12 μm, which were identified as the epsilon-near-zero (via Berreman modes) and maximum-negative-permittivity (via photon-tunneling modes) wavelengths of SiO_2 and AlO_X, respectively, thus supporting phonon−polariton resonance mediated broadband side emission. As proof-of-concept experiments, we demonstrated that these exceptional epsilon-based microcavities could provide thermal comfort to users and practical cooling performance to optoelectronic devices.

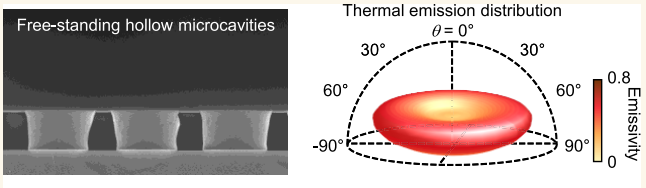

KEYWORDS: *Midinfrared photonics, directional thermal emission, radiative cooling, Bayesian optimization, Berreman mode*

Blackbody radiation features a highly asymmetric, continuous spectrum that relies exclusively on the surface temperature.[1,2] Planck's law describes that thermal emission peaks at a characteristic wavelength that is blueshifted with increasing temperature. Consequently, a blackbody at room temperature (*e.g.*, 300 K) radiates nearly half of the electromagnetic energy in the atmospheric window (8−14 μm).[1,3] Once considered an elusive task, molding the spectrum of thermal emission in the frequency or momentum domain is now conceivable owing to advances in nanophotonics.[2,3] For real objects in local thermal equilibrium, Kirchhoff's law of thermal radiation (i.e., emissivity (ε) equals absorptivity (α)) still holds at every combinatorial specific set of wavelength (λ), angle (θ), and polarization (p). Then, nanophotonics is capable of adjusting ε at selected λ, θ, and p using the concepts of photonic crystals,[4−6] plasmonic gratings,[7−10] hyperbolic metamaterials,[11,12] multilayer interference coatings,[13−17] Mie scattering,[18,19] and Fabry−Perot resonances.[20]

To date, much attention has been paid to accomplishing wavelength-selective thermal emission, which supports the development of thermophotovoltaics,[5,6,11,13] radiative coolers,[10,12,14−16,20] and infrared camouflaging.[17] In the era of carbon neutrality, radiative coolers are garnering increasing popularity because they do not consume external energy for cooling[1,3] and are formed as scalable thin films.[12,14−16] In addition, their practical function can be adaptively switched between cooling and heating with the use of temperature-triggered emissivity-changing materials (*e.g.*, vanadium oxide) to override excessive cooling in cold settings.[21,22] In comparison, angle-selective thermal emission is more challenging because of the complexity of design principles.[7,8] For example, Greffet et al. reported narrow-angle emission at a single thermal wavelength (11.36 μm) in the p polarization by constructing a one-dimensional (1D) wavelength-scale grating (6.25 μm in pitch) on a SiC substrate.[7] Such a plasmonic grating provides near-unity, directional emission at the desired wavelength under a stringent amplitude-bandwidth constraint. Argyropoulos et al. theoretically showed broadband (5−10 μm), polarized angular thermal emission using a 1D tapered metal grating with a depth of 9.1 μm;[8] however, its fabrication is very complex. More recently, Xu et al. demonstrated broadband (7.7−11.5 or 10.0−14.3 μm) directional thermal

Received: February 7, 2023
Accepted: May 15, 2023
Published: May 18, 2023

https://doi.org/10.1021/acsnano.3c01184
ACS Nano 2023, 17, 10442−10451

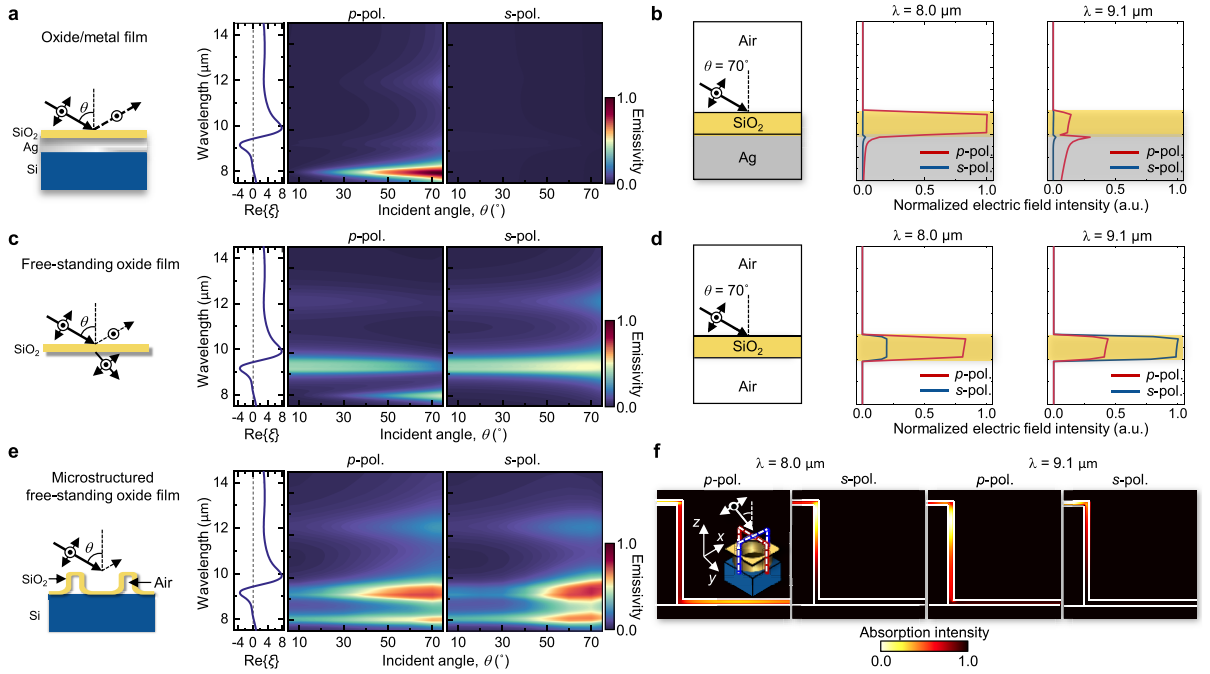

Figure 1. Oxide-based thermal emitters. (a–f) Simulated energy–momentum dispersions and electromagnetic energy distributions of an oxide/metal film (a,b), a free-standing oxide film (c,d), and a microstructured free-standing oxide film (e,f). (a–f) The SiO_2 thickness is 100 nm, and the material dispersion (i.e., the real part of the permittivity, Re{ξ}) of SiO_2 is also plotted. In the material dispersion plot, the dashed line indicates zero permittivity. (b,d) The energy distributions are obtained at 8 (left) and 9.1 μm (right) for both p and s polarizations with θ = 70°, which are normalized with the result of the oxide/metal film structure at 8.0 μm in the p polarization. (f) Absorption profiles of a microstructured free-standing oxide film (100-nm-thick SiO_2). These are obtained at 8.0 (left) and 9.1 μm (right) in the p and s polarizations when θ = 70°. Each profile is obtained by spatial averaging of the absorption intensity values for the *xz* and *yz* cross sections.

emitters, using gradient epsilon-near-zero (ENZ) thin films consisting of multiple oxides on a metal mirror.[17] Notably, the coupling of light in free space to Berreman modes at ENZ wavelengths occurs only in the p polarization because the permittivity of an oxide vanishes at its longitudinal optical (LO) phonon frequency.[23−27] As a result, the gradient ENZ films had prominent ε values at large off-angles (*e.g.*, 74° or 64°) in the p polarization, whereas their ε values in the s polarization were constantly low (ε < 0.2) in the entire angle range.[17] Overall, previous approaches were successful for a limited spectrum or specific polarization.[7,8,17] Their angular selectivity became modest when averaged throughout the entire spectrum (*e.g.*, 8−14 μm for radiative coolers) and in the two orthogonal polarizations. Therefore, their total hemispherical emissivity (ε_T) values considered over all solid angles were vanishingly small (*e.g.*, $\varepsilon_T \sim 0.2$),[17] and hence substantial radiative cooling effects have not yet been reported. Moreover, the practical uses of directional thermal emitters or radiative coolers have remained unclarified.

Here, we report a broadband, directional radiative cooler that features high-amplitude side emission in both the p and s polarizations. Microstructured, free-standing oxide films were proposed, and their multidimensional structural variables were tuned with Bayesian optimization to maximize the angular selectivity and ε_T in the target spectrum. A designer structure was precisely fabricated using standard semiconductor processes. Energy–momentum dispersions were acquired to unravel the underlying physics of the directional emission that peaked at multiple exceptional epsilon wavelengths. In principle, an omnidirectional thermal emitter provides a more efficient way of cooling in an open system,[12,14−16,20] compared with a directional thermal emitter that restricts its emission in a certain range of angles. However, we note that an omnidirectional thermal emitter can be ineffective in a closed system[28,29] because of the greenhouse effect.[29] In comparison, our proof-of-concept experiments demonstrated that the developed side-emission thermal emitter maintained cooling performance even in a closed system. In addition, it could provide thermal comfort for the user near optoelectronic devices.

RESULTS AND DISCUSSION

Phonon–Polariton Resonance Mediated Directional Thermal Emission. A Berreman configuration, which consists of a deep-subwavelength-thickness oxide film on a metal mirror,[26] initiates a motif to design our directional thermal emitter. To access the Berreman mode that exhibits a prominent maximum ε at LO phonon resonance, the ideal thickness (t_B) of the oxide film is determined as follows:[26]

$$t_B = \frac{\lambda}{2\pi}\frac{\cos\theta}{\sin^2\theta}[\mathrm{Im}\{-1/\xi(\lambda)\}]^{-1}_{\max}$$

where λ is the wavelength of the LO phonon resonance, $\xi(\lambda)$ is the permittivity function of the oxide film, and θ is the angle of incidence. We obtained the angle-resolved emissivity spectrum (i.e., energy–momentum dispersion) of 100-nm-thick SiO_2 on a Ag mirror ($t_B \sim$ 100 nm at 70° incidence), using a rigorous coupled-wave analysis (RCWA) simulation (Figure 1a). The oxide/metal film confines its thermal emission to glancing angles at an ENZ wavelength (*e.g.*, 8 μm for SiO_2) exclusively in the p polarization, which is a clear sign of the Berreman

https://doi.org/10.1021/acsnano.3c01184
ACS Nano 2023, 17, 10442−10451

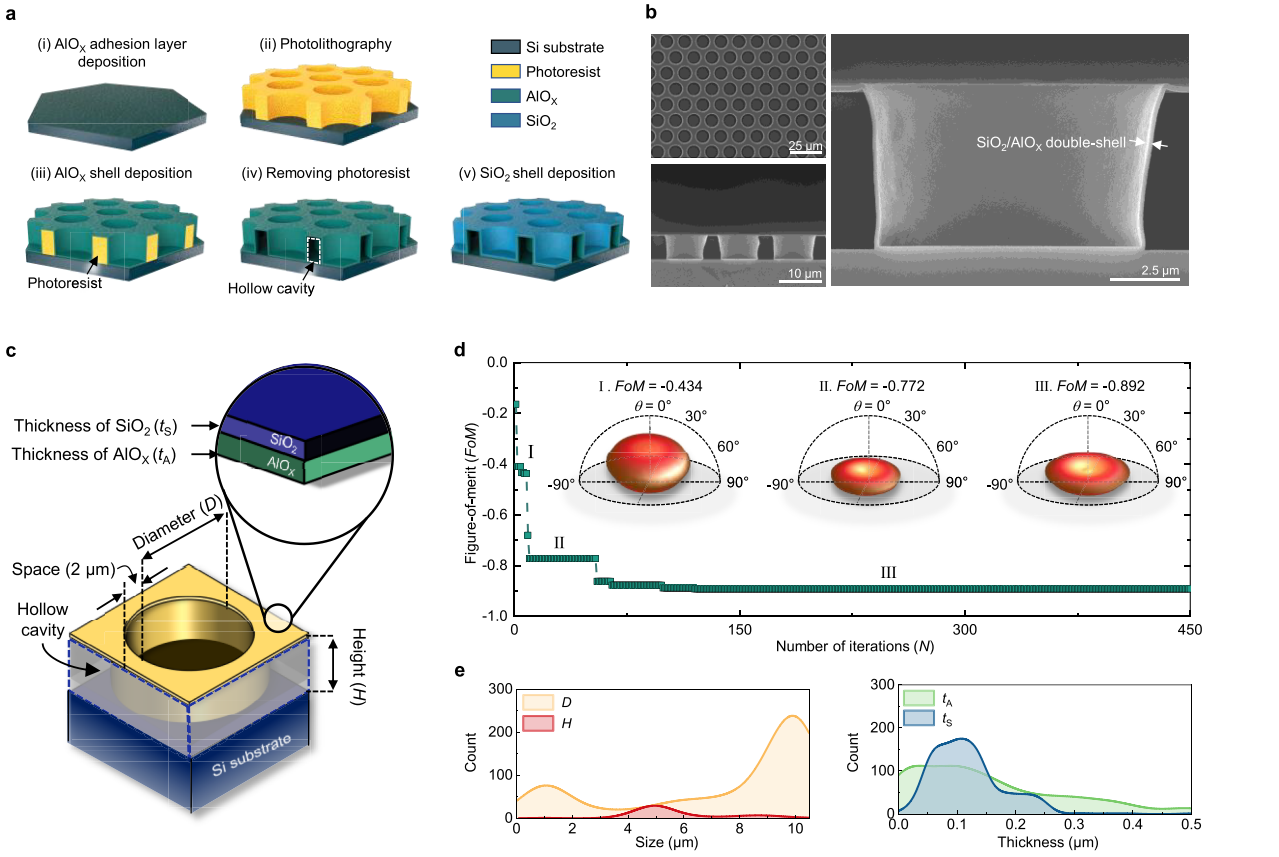

Figure 2. Design and fabrication of SiO_2/AlO_X double-shell hollow microcavities (HMs). (a,b) Schematic illustrating the fabrication process (a) and scanning electron microscopy (SEM) images (b) of an array of SiO_2/AlO_X double-shell HMs. (c–e) Bayesian optimization for designing SiO_2/AlO_X double-shell HMs. (c) Schematic of a simulated structure for the optimization. The space is fixed to 2 μm. (d) History of the minimum figure-of-merit (FoM) values with increasing *N*. (Inset) Far-field distributions of thermal emission for specific local minimum domains: first (I), intermediate (II), and final (III) stages. (e) Parametric distribution curves throughout the total number of iterations.

mode.[25,26] To better comprehend the Berreman mode, we obtained the electromagnetic energy distribution of the same structure (Figure 1b). At 8 μm (i.e., an ENZ wavelength), a p-polarized plane wave with a large in-plane wave vector (*e.g.*, 70° incidence) is tightly trapped in the ultrathin SiO_2 film. At the ENZ wavelength, the absorption/emission amplitude is dramatically enhanced because the real part of the SiO_2's permittivity vanishes, which is given as follows:

$$\varepsilon(\lambda) = \frac{\pi c}{\lambda}\mathrm{Im}\{\xi(\lambda)\}|E_0(\lambda)/\mathrm{Re}\{\xi(\lambda)\}|^2$$

where c is the speed of light, λ is an ENZ wavelength, $E_0(\lambda)$ is the electric field in free space, and $\mathrm{Re}\{\xi(\lambda)\}$ and $\mathrm{Im}\{\xi(\lambda)\}$ are the real and imaginary parts of an oxide's permittivity function, respectively. This field localization accounts for the high-amplitude emission band.[23]

In comparison, for a free-standing SiO_2 film with the same thickness, two different emission bands emerge at 9.1 and 12.5 μm in both the p and s polarizations, in addition to the Berreman mode in the p polarization (Figure 1c). The former (9.1 μm) is assigned to a photon-tunneling mode because it appears at the maximum-negative-permittivity wavelength,[20] where the transverse optical (TO) phonon resonance of SiO_2 coincides. The photon-tunneling mode induces nearly omnidirectional thermal emission, irrespective of the polarization. Its energy distribution is highly localized in the suspended SiO_2 film for the two orthogonal polarizations (Figure 1d). The Berreman mode is still identified at 8 μm in the p polarization, albeit having a slightly lower amplitude. Fundamentally, the emission bands at 8 and 9.1 μm result from the coupling of photons and the "asymmetric" stretching vibration of SiO_2.[30] The free-standing oxide film exhibits a modest but broadened emission band at 12.5 μm, which is associated with the "symmetric" stretching vibration of SiO_2.[31] Consequently, it supports three distinct emission bands at 8, 9.1, and 12.5 μm in a single-layer film configuration, although the Berreman mode in the p polarization solely contributes to directional thermal emission.

For this study, we propose a "microstructured" free-standing SiO_2 film, namely, an array of SiO_2-shell hollow microcavities (HMs; Figure 1e). This structure has the three emission bands at 8, 9.1, and 12.5 μm in both the p and s polarizations. More importantly, their amplitudes are significantly augmented at large off angles (50–75°). To confirm the polarization-irrelevant behavior, we obtained the energy distributions (in terms of absorption profiles, averaged for the *xz* and *yz* cross sections) of SiO_2-shell HMs at 8 and 9.1 μm (Figure 1f). For the 70° incidence, both the p- and s-polarized plane waves are entirely absorbed in the SiO_2 shell, which is due to its three-dimensional nature. At λ = 8 μm (i.e., epsilon-near-zero wavelength), the electric field with respect to the *xz* plane is highly confined in the top and bottom shells in the p

https://doi.org/10.1021/acsnano.3c01184
ACS Nano 2023, 17, 10442–10451

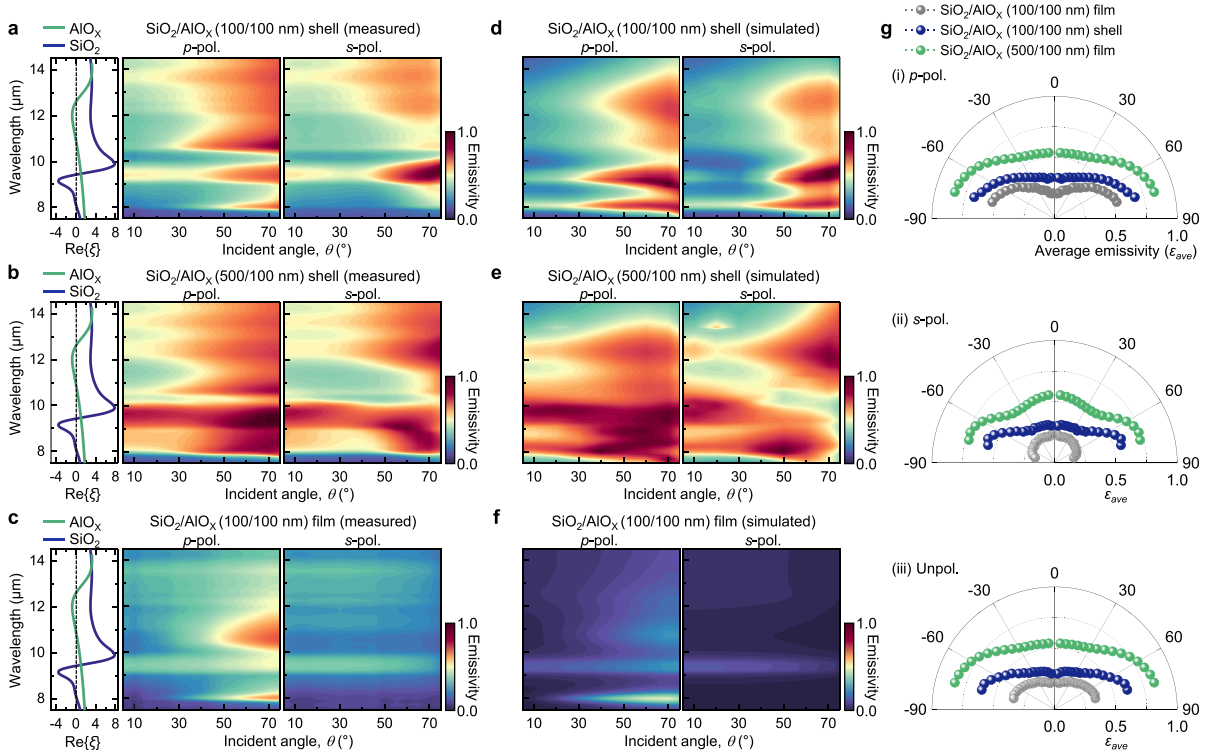

Figure 3. Measured and simulated energy−momentum dispersions. (a−f) Measured (a−c) and simulated (d−f) energy−momentum dispersions in the p and s polarizations for (a,d) SiO_2/AlO_X (100/100 nm), (b,e) double-shell HMs (500/100 nm), and (c,f) bilayer film (100/100 nm). In the material dispersion plot, the dashed line indicates zero permittivity. (g) Polar plots exhibiting ε_{av} values obtained from the results of a−c. Each value is weighted by the 300 K blackbody spectra.

polarization. In comparison, in the s polarization, the electric field with respect to the *yz* plane is strongly localized in the side shell. Likewise, at λ = 9.1 μm (i.e., maximum-negative-permittivity wavelength), the electric field was relatively intense in the side (in the p polarization) or top (in the s polarization) shells, depending on the state of polarization. Since the mode at λ = 9.1 μm is identified as the TO phonon resonance of SiO_2, the maximum field confinement appears in reverse with respect to polarization compared to the mode at λ = 8 μm stemming from the LO phonon resonance, as demonstrated by Figure 1d. These findings account for the high-amplitude emission bands at 8 and 9.1 μm in both the p and s polarizations (Figure 1e) as compared to the flat film (Figure 1c). We emphasize that the intensified side emission is attained only with hollow (as opposed to dielectric) microcavities because such phonon−polariton resonances rely heavily on the boundary conditions of interfaces (*e.g.*, air/oxide/air).[25,31] For more quantitative understanding, the emissivity values of microcavities at the wavelengths corresponding to ENZ (λ = 8 μm) and maximum-negative-permittivity (λ = 9.1 μm) values of SiO_2 for 0° and 70° incidences when filled with materials having varying complex refractive indices ($n + ik$) were mapped in the Supporting Information, Figure S1a,b. Each plot was averaged in both polarizations. We presented surface plots and marked the emissivity values for several well-known materials such as SiO_2, ZnS, and Si. Our analysis indicates that the emissivity of the microcavity structure was reduced at θ = 0° when filled with nonabsorbing materials. Furthermore, the hollow microcavity (*i.e.*, n = 1.0) was situated near a high-amplitude plateau in each θ = 70° plot. The average emissivity (ε_{av}) values of the microcavity structures hollow and filled with SiO_2, ZnS, and Si as a function of θ support the results presented in Supporting Information Figure S1a,b (Supporting Information Figure S1c). For example, for ZnS (as an infrared transparent material[15]) microcavities with a 100-nm-thick SiO_2 shell, an incident plane wave considerably dissipates through the ZnS microcavities, thus reducing ε at large off angles (Supporting Information Figure S1d).

Design and Fabrication of Exceptional Epsilon-Based Hollow Microcavities. We employed an additional AlO_X shell to achieve directional thermal emission at broad wavelengths (8−14 μm), which is a critical wavelength band for radiative cooling[1] and infrared imaging,[9] because the LO and TO phonon resonances of AlO_X are discretely spaced at 10.9 and 12 μm, respectively.[32] Overall, the same trend as in the SiO_2 examples recurs; the AlO_X-shell HMs support the Berreman mode and photon-tunneling mode in the p and s polarizations, creating angle-selective emission bands (Supporting Information Figure S2). AlO_X has a relatively flattened material dispersion, which compensates adequately for the interband emissivity throughout 10−14 μm. SiC is also a good candidate material to incur side thermal emission via Berreman mode.[27] In Supporting Information Figure S3a, we plotted the material dispersion of SiC and energy-momentum dispersion for a 100-nm-thick SiC layer on an Ag mirror. We observed a high-amplitude band at the epsilon-near-zero wavelength of SiC, which is the same trend seen in the SiO_2 and AlO_X examples (Figure 1 and Supporting Information Figure S2).

Wet etching, thin film deposition, and photolithography—all standard semiconductor processes—were used to create an array of SiO_2/AlO_X double-shell HMs (see Materials and

https://doi.org/10.1021/acsnano.3c01184
ACS Nano 2023, 17, 10442−10451

Methods, Figure 2a).[33] This fabrication did not undergo plasma etching for micron-depth patterning; instead, the thickness of the photoresist in use directly determined the height of HMs. Scanning electron microscopy (SEM) images revealed that HMs were clearly formed without any inner residual photoresist, sustained by the heterogeneous oxide shells (Figure 2b and Supporting Information Figure S4).

The double-shell HMs were characterized by four key variables: diameter (D), height (H), and AlO_X (t_A) and SiO_2 thicknesses (t_S; Figure 2c). Variations of D and H should be investigated across 1−10 and 1−15 μm, respectively. In addition, the range of t_A and t_S should be 0.01−0.5 μm. Consequently, a traditional forward design requires 66 671 computations per a single set of wavelength and angle, assuming that the scan steps for (D, H) and (t_A, t_S) are 0.5 and 0.05 μm, respectively. This becomes exceedingly troublesome when exploring a broad range of wavelengths (8−14 μm) and angles (0°−80°) with fine increments. To mitigate such difficulty, we used Bayesian optimization[34] to address the four-variable design problem (see Materials and Methods), thus promptly determining a desired directional thermal emitter. For optimization, we defined a figure-of-merit (FoM) as follows:

$$\mathrm{FoM} = -\left(\frac{\varepsilon_{70}}{\varepsilon_0}\right)(\varepsilon_{70} - \varepsilon_0)$$

where ε_{70} and ε_0 represent ε values for 70° and 0° incidences, respectively, averaged at the four primary wavelengths of 8, 9.1, 10.9, and 12 μm for two orthogonal polarizations because both angular selectivity and emissivity values are locally maximized at those wavelengths, as demonstrated in Figure 1e and Supporting Information Figure S2. As discussed in Supporting Information Figure S1a−c, both angular selectivity and emissivity values were pronounced with the hollow microcavity structure. In these simulations, we also considered two phonon mode wavelengths (i.e., ENZ and the maximum-negative-permittivity wavelength of SiO_2) for different incident angles of 0° and 70°. We confirmed that the average emissivity (ε_{av}) plots qualitatively support these results (Supporting Information Figure S1c), which reveals the feasibility of the design rule using the four exceptional epsilon wavelengths of SiO_2 and AlO_X. We plotted the history of the minimum FoM with respect to the number of iterations (N; Figure 2d). An expected global minimum was discovered only after $N > 120$. We obtained far-field distributions of thermal emission at every local minimum domain (inset, Figure 2d). The emission pattern was almost omnidirectional at the first onset (I). Although it was directional at the intermediate stage (II), the side emission had a low amplitude. At the final stage (III), high-amplitude, directional emission was observed. The optimal variable set of (D, H, t_A, t_S) is (10, 5.1, 0.1, 0.13) μm, which is derived from the peak of each parametric distribution curve (Figure 2e). Notably, the Bayesian optimization correctly recognizes that the glancing-angle emission is achieved when the oxide shell thicknesses are at deep-subwavelength scales.

Measured and Simulated Energy−Momentum Dispersions. We obtained the energy−momentum dispersion of a fabricated SiO_2/AlO_X (100/100 nm) double-shell HM array to characterize the spectral and angular responses (Figure 3a). Its structural variables (D, H, t_A, and t_S) are consistent with those determined from the Bayesian optimization. For references, we fabricated a SiO_2/AlO_X (500/100 nm) double-shell HM structure and SiO_2/AlO_X (100/100 nm) bilayer film (Figures 3b,c). The former was prepared to investigate the impact of an oxide-shell thickness, whereas the latter was used to validate the superiority of the structured free-standing film. The SiO_2/AlO_X (100/100 nm) double-shell sample induced pronounced, directional emission, with peaks at 8, 9.1, 10.9, and 12 μm, which sequentially correspond to the ENZ and maximum negative permittivity wavelengths of SiO_2 (8 and 9.1 μm) and AlO_X (10.9 and 12 μm), respectively. In addition, the different type of phonon resonance of SiO_2, which is excited at approximately 12.5 μm, contributed to the broadband directional emission, as observed in Figure 1e. We note that the SiO_2 and AlO_X shells work in tandem as an independent mode. Thus, the energy−momentum dispersion represents a superposition of that of each oxide-shell structure. The energy-momentum dispersion remains unaffected by the configuration of the SiO_2 and AlO_X shell (i.e., SiO_2/AlO_X and AlO_X/SiO_2 double shells), as shown in Supporting Information Figure S5. In the experiment, we chose AlO_X as the inner shell material due to its compatibility with atomic layer deposition, which facilitates the fabrication of hollow microcavities. While the SiO_2/AlO_X (500/100 nm) double-shell sample significantly amplifies each emission band owing to the increased t_S, its angular selectivity rather decreases (Figure 3b). The SiO_2/AlO_X (100/100 nm) bilayer sample provides directional emission bands only at the ENZ wavelengths (8 and 10.9 μm) of each oxide in the p polarization (Figure 3c), which accounts for the characteristics of the Berreman mode.[24−26]

To verify the measured results, we simulated energy−momentum dispersions of the considered samples (Figure 3d−f). The simulated and measured results were in good agreement in terms of peak wavelength and amplitude. However, for the SiO_2/AlO_X (100/100 nm) double-shell sample, the emission band at 8 μm in the s polarization almost vanished in the measurement. The ENZ-based emission primarily emanates from the sidewalls of the SiO_2 shell (Figure 1f). However, the ultrathin SiO_2 shell was not sufficiently conformal during the plasma-enhanced chemical vapor deposition (PECVD) process, and thus its sidewall thickness was nominal (Supporting Information Figure S4).

To facilitate a quantitative comparison, we obtained spectrally averaged (8−14 μm) emissivity (ε_{av}) values of each sample using its measured energy−momentum dispersion while altering the incident angles (θ) in the p and s polarizations (see Materials and Methods, Figure 3g). The data from previously reported gradient ENZ thin films,[17] which are considered to be state-of-the-art in terms of broadband directional thermal emission, were plotted together in Supporting Information Figure S6. In stark contrast with the planar film sample, both hollow cavity samples exhibited angle-selective emissions to varying degrees in the p and s polarizations (Figure 3g). The angular selectivity became pronounced in the thinner shell sample. The SiO_2/AlO_X (100/100 nm) double-shell sample provided emissivity values of 0.31 and 0.56 when averaging ε_{av} over 5−20° and 60−75°, respectively. In comparison, the emissivity values of the SiO_2/AlO_X (500/100 nm) double-shell sample were 0.58 and 0.78 for the near-normal and glancing incidences, respectively. The thicker SiO_2 shell augmented ε_T (0.69 for the thicker shell sample and 0.47 for the thinner shell sample; Supporting Information Table S1), which enhanced the radiative cooling capability at the cost of angular selectivity.

https://doi.org/10.1021/acsnano.3c01184
ACS Nano 2023, 17, 10442−10451

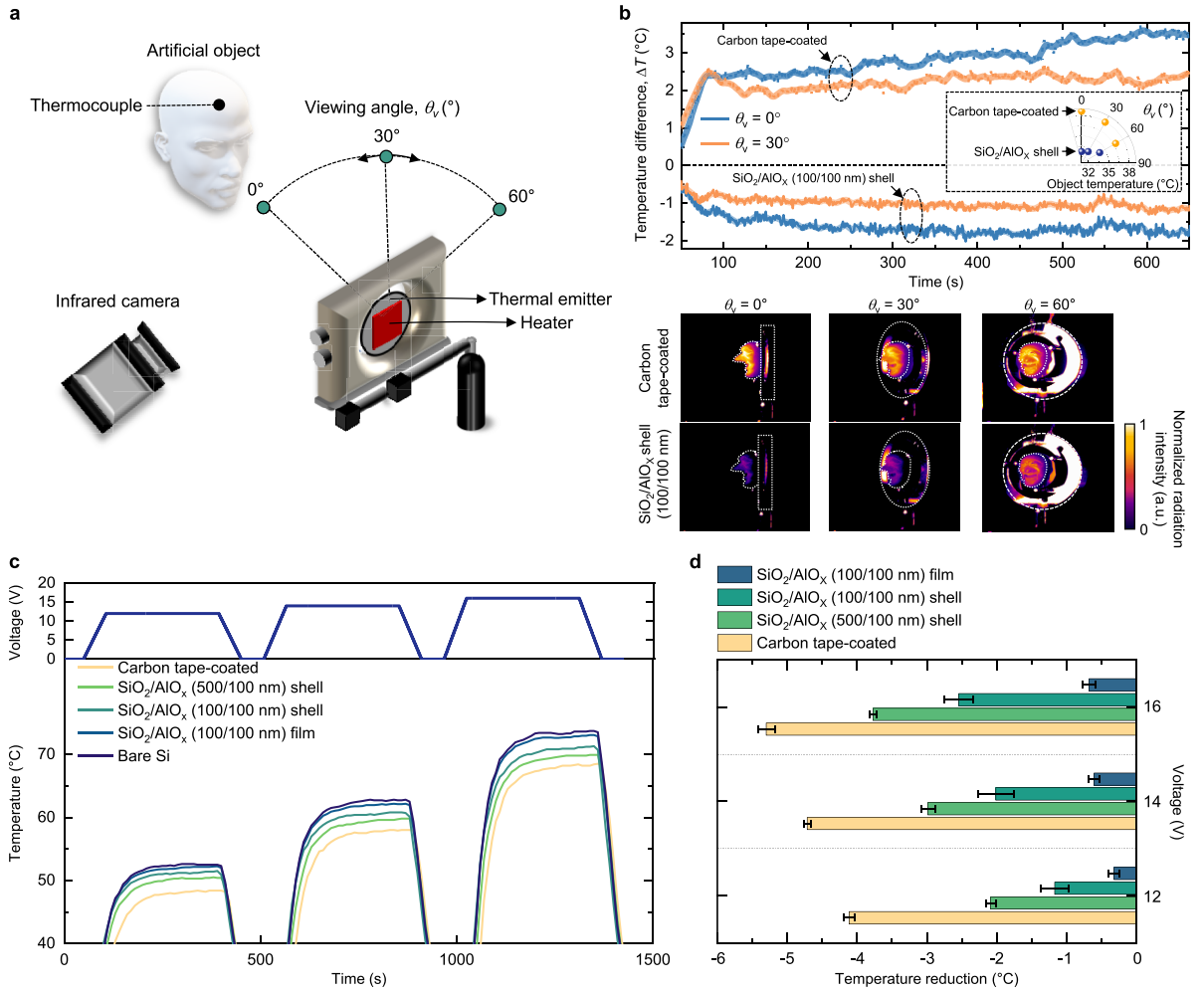

Figure 4. Thermal comfort and radiative cooling experiments. (a,b) Thermal comfort experiments. (a) Schematic of the experimental setup. Each sample (i.e., SiO_2/AlOx (100/100 nm) double-shell HMs and carbon tape-coated Si) is attached to an electric heater at 100 °C. (b) Temporal change of ΔT values (upper panel) and infrared thermography images (lower panel). ΔT is defined as the difference between the temperature at θ_v = 60° and θ_v = 0° or 30°. (Inset) Angular distribution of the object temperature for the SiO_2/AlO_X (100/100 nm) double-shell HMs and carbon tape-coated Si. The infrared thermography images are normalized with the maximum intensity of the carbon tape-coated mask for θ_v = 0°. (c,d) Radiative cooling experiments. (c) Temporal change in temperature for each sample. (Upper panel) Time-varying input voltage signals. (d) Temperature reduction values with respect to the bare Si at 12, 14, and 16 V. The error bars represent standard deviation values obtained 30 s before the end of each cycle over three independent measurements.

Thermal Comfort and Radiative Cooling Experiments. We further conducted two proof-of-concept experiments with the developed broadband directional thermal emitters, one related to thermal comfort[35] and the other to radiative cooling.[1] As the operating temperature of personal displays such as smartphones and virtual reality headsets is elevated, a strategy for avoiding thermal emission from a device to a user can be crucial.[36,37] First, we devised a thermal comfort experiment to emulate a setting of personal displays, in which a thermally black object (i.e., a person's face) revolved around a thermal emitter connected to a 100 °C electrical heater (see Materials and Methods, Figure 4a). For the proof-of-concept experiment, the distance from the black object to thermal emitter was 7.5 cm to emulate the situation of near-distance applications, such as smartphones and virtual reality headsets. The SiO_2/AlO_X (100/100 nm) HM sample in Figure 3 was used for the thermal emitter. As a reference, carbon tape was used because it behaves as a near-perfect blackbody with omnidirectional emission distribution (ε_T = 0.92, Supporting Information Table 1), as is the case for most cover window materials (*e.g.*, glass or polyimide) of optoelectronic devices. We recorded the temperature of the artificial face using a thermocouple at three different viewing angles (θ_v = 0°, 30°, and 60°) and plotted the temperature difference (ΔT) values between θ_v = 60° and 0° or 30° (upper panel, Figure 4b). For the carbon tape emitter, ΔT was positive (ΔT > 2 °C) at θ_v = 0° and 30°, indicating that the warmth of the artificial face rises more when viewed from the front than the side. In contrast, ΔT was negative (ΔT < −1 °C) for our HM emitter, showing its directional emission distribution. It should be noted that the directional emission of our HM emitter is verified by the angular distribution of the object temperature, which is consistent with Figure 2g (inset, Figure 4b). Longwave (7.5−13.5 μm) infrared thermography supported the variation of the measured ΔT values (lower panel, Figure 4b). In our experimental setup, the view factor was approximately 0.21.[38] We postulate that the object temperature can drastically increase as the view factor is larger,[29] leading to increased temperature differences at each viewing angle. With the SiO_2/AlO_X (100/100 nm) double-shell HM emitter, the artificial

https://doi.org/10.1021/acsnano.3c01184
ACS Nano 2023, 17, 10442−10451

face was concealed at normal incidence, whereas it was identified at 60° incidence (i.e., angle-selective infrared camouflaging;[17] lower panel, Figure 4b and Supporting Information Figure S3). These findings suggest that such a directional thermal emitter can keep a user cool even when the user is in close proximity to a heating device.

Next, we conducted a radiative cooling experiment using an external electrical heater (see Materials and Methods, Figure 4c). The temporal changes in temperatures of the bottom surface of Si substrates were recorded while the electrical heater supplied thermal energy to the Si substrate at different bias voltages. The Si substrates were coated with the four different thermal emitters, as presented in Figure 4c. The temperature reduction induced by the thermal emitters was clearly ranked in order of their ε_T values (Figure 4d and Supporting Information Table S1); the carbon tape emitter exhibited the greatest cooling performance. More importantly, compared to the bilayer film emitter, both HM emitters provided a decent level of thermal capability. Consequently, we could customize thermal responses spectrally and spatially based on the developed HM platform by adjusting the thickness and composition of the oxide shells. Reiterating the general guideline, a thicker oxide shell benefits radiative cooling at the expense of thermal comfort.

CONCLUSIONS

We demonstrated directional thermal emission, using SiO_2/AlO_X double-shell HMs with their multidimensional structural variables tailored via Bayesian optimization. Free-standing oxide films support multiple emission bands at discrete infrared wavelengths, where the real part of the oxide's permittivity is zero or maximum negative. When they are appropriately structured (i.e., with an array of HMs), their emissivity becomes dramatically enhanced at large off angles. The angular selectivity is nearly equal in the p and s polarizations on account of the three-dimensional nature of HMs. The double-shell materials, SiO_2 and AlO_X, with their TO and LO phonon resonances sequentially spaced between 8 and 14 μm, enable broadband performance. As a result, the developed SiO_2/AlO_X double-shell HMs provide practical functionalities that can relieve the thermal discomfort of users and release the thermal energy of devices. The addition of a third oxide shell, such as TiO_2, which adjoins the thermal emission bands of the SiO_2/AlO_X double-shell HMs beyond 8−14 μm, can broaden the bandwidth of directional thermal emission, thereby enhancing thermal functionalities. Furthermore, directional thermal emission can be achieved in the near-infrared (1−2 μm) for high-temperature (>800 °C) objects when indium tin oxide[39] and cadmium oxide[13] are employed as shell materials.

The broadband directional emission stems mainly from the strong coupling of photons and exceptional epsilon-based HMs. Additional statistical analysis with Bayesian optimization exhibited only a marginal variation within the range of $2 < D < 12$ μm, which is indicative of the fabrication tolerance of these HMs (Supporting Information Figure S8). These findings further suggest that the strong coupling of photons and exceptional epsilon-based HMs persists even on large scales. In our previous study,[20] we observed that HMs retained their properties at high temperatures above 1000 K under atmosphereic pressure. However, an assessment of their mechanical robustness is a remaining mission. We postulate that oxide-based shells could potentially be substituted with soft polymer materials (*e.g.*, polydimethylsiloxane). However, a crucial criterion for the selection of shell materials will be necessary to resist their dissolution in the acetone-based wet-etching process. When used in display applications to maintain thermal comfort, the periodic array of HMs causes diffraction of light, which diminishes visibility. This problem could be resolved by arranging HMs at random, which can improve specular transparency in the visible. Moreover, radiative cooling based on directional thermal emission is more effective in a closed configuration, where the top cover returns some of the thermal energy generated by the heating device to itself (Supporting Information Figure S9). This alleviates the greenhouse effect,[29] suggesting a strategy for radiative cooling in a closed system.[28,29] Directional radiative coolers typically emit thermal energy in a vertical orientation, capitalizing on the angle-dependent transmittance of the atmospheric window. Consequently, the developed side-emission thermal emitters hold the promise of facilitating radiative cooling for the sidewalls of buildings and building integrated photovoltaics.[40] Finally, ENZ-material-covered optical resonators produce a strong light−matter interaction, which can be leveraged to achieve perfect light absorption[41] and enhance nonlinear effects.[42]

MATERIALS AND METHODS

Fabrication of Directional Thermal Emitters. SiO_2/AlO_X (100/100 nm) double-shell hollow microcavities (HMs) were fabricated by performing photolithography on double-side-polished p-doped crystalline Si wafers (*e.g.*, 2 in. in diameter). For the Si wafers, we used high-resistivity (1 kΩ·cm) wafers to minimize the free-carrier absorption at mid-infrared wavelengths. A 150-nm-thick Ag layer was first evaporated on the backside of the Si wafer as a reflector using an electron beam evaporator (UEE, ULTEC). Then, a 10-nm-thick AlO_X adhesion layer was deposited on the top side of the Si wafer using atomic layer deposition (ALD; LUCIDA D100, NCD) as an adhesion layer. To construct a micron-depth optical cavity structure, a photolithography process was conducted. First, 5-μm-thick AZ 4620 positive photoresist was coated on the top side of the Si wafer, followed by ultraviolet exposure under a chrome photomask in a mask aligner (MA-150e, Karl Suss). For conformal deposition along the patterned photoresist, the ALD technique was performed to construct the AlO_X (100 nm) inner shell. The AlO_X-coated patterned photoresist was removed by dipping into an acetone solution (99%, Sigma-Aldrich), followed by a thermal annealing process at 800 °C for 3 h to remove the photoresist residue. Additionally, a SiO_2 (100 nm) shell was deposited for the outer shell using plasma-enhanced chemical vapor deposition (VL-LA-PECVD, Unaxis). Cross-section scanning electron microscopy (S4800, Hitachi High-Tech) exhibited well-defined SiO_2/AlO_X (100/100 nm) double-shell HMs.

Optical Characterization. The variable-angle absorptivity/emissivity spectra were obtained using a Fourier-transform of infrared (FTIR) spectrometer (INVENIO R, Bruker) equipped with a variable-angle accessory (Harrick Seagull). To acquire absorptivity/emissivity spectra with s and p polarization, a ZnSe holographic wire grid polarizer (WP50H-Z, Thorlabs) was employed. The average (λ = 8−14 μm) emissivity (ε_{av}) at an incidence angle of θ, weighted by the blackbody spectra at 300 K, is expressed as follows:

$$\varepsilon_{av} = \frac{\int_8^{14} \varepsilon(\lambda, \theta) I_{BB}(T, \lambda)\, d\lambda}{\int_8^{14} I_{BB}(T, \lambda)\, d\lambda}$$

Here, $\varepsilon(\lambda, \theta)$ is the measured emissivity at an incidence angle of θ. Additionally,

$$I_{BB}(T, \lambda) = \frac{2hc^2}{\lambda^5} \frac{1}{e^{hc/(\lambda k_B T)} - 1}$$

https://doi.org/10.1021/acsnano.3c01184
ACS Nano 2023, 17, 10442−10451

is the spectral radiance of a blackbody at temperature T, where h is Planck's constant, k_B is the Boltzmann constant, c is the speed of light in a vacuum, and λ is the wavelength.

Electromagnetic Simulations. Simulations of absorptivity/emissivity spectra were conducted using rigorous coupled-wave analysis (RCWA; DiffractMOD, Rsoft). To elucidate deep sub-wavelength-thick oxides, we set the harmonics and z-resolution values to 16 and 5 nm, respectively. Further, electromagnetic energy distribution profiles were obtained from the home-built finite-difference time-domain (FDTD) program. A spatial resolution of 10 nm was used for all the x-, y-, and z-coordinates in all of the simulation models. The AlO_X and SiO_2 material dispersion were derived from refs 30 and 32. For simplicity, the Si wafers had a nondispersive optical constant of n = 3.5 at the mid-infrared wavelengths (5−15 μm).[20] For ZnS-filled microcavities, the ZnS material dispersion was obtained from ref 15.

Bayesian Optimization. Bayesian optimization (BO) is a sequentially performed, global optimization method based on the statistical evaluation of an optimized function.[34] BO consists of the following steps: (i) BO builds a surrogate model based on the Gaussian process regression (GPR) with a data set that includes input parameters (*e.g.*, D, H, t_A, and t_S) and associated output values (*e.g.*, figure-of-merit, FoM). (ii) BO estimates the score of a cost pave function (i.e., acquisition function) based on the surrogate model to gauge the next values of parameters for the optimization. (iii) A new data set is updated after estimating the FoM with these suggested input parameters. (iv) BO builds a more accurate surrogate model by repeating the sequential steps of i, ii, and iii (it can be referred to as one iteration), and (v) finally, with a sufficient number of iterations (N), BO finds the optimal values of the input parameters that yield the best output values. In this study, BO uses Scikit-learn[43] for the GPR with the kernel of anisotropic radial basis function (RBF, i.e., squared-exponential kernel),[44] and it employs the expected improvement for the cost function. It is noted that the anisotropic RBF has four length scales for each of the D, H, t_A, and t_S parameters. The initial calculation starts with 20 sets of input parameters (D, H, t_A, and t_S) and the associated output (FoM), where each value of the input parameters is randomly sampled in the following ranges: 1 μm < D < 10 μm, 1 μm < H < 15 μm, 0.01 μm < t_A < 0.5 μm, and 0.01 μm < t_S < 0.5 μm. We performed BO with N > 400, thus ensuring that the best values of input parameters were found (i.e., an expected global optimum of FoM).

Thermal Comfort Experiments. As a proof of concept, a thermal comfort experiment was conducted in which a thermally black object was revolved around a thermal emitter at a distance of 7.5 cm. The temporal variations in temperature were recorded on the top surface of the object using adhesive thermocouples (SA1-K-72, Omega Engineering) at three different viewing angles (*i.e.*, θ_v = 0°, 30°, and 60°). The measurements were recorded at intervals of 10 s on a data logger (RDXL 12 SD, Omega Engineering). We used SiO_2/AlO_X (100/100 nm) double-shell HMs and carbon-tape-coated Si as the thermal emitter for each measurement. The thermal emitter was connected to the electrical heater, which maintained its temperature (i.e., 100 °C) through a proportional-integral-derivative controller.

The longwave infrared thermography images were obtained using an infrared camera (FLIR A655SC). The spectral range of the thermal camera was 7.5−13.5 μm. Each image was calibrated to a carbon-tape-coated Si wafer as a reference. In addition, p- and s-polarized infrared images were acquired by placing a ZnSe holographic wire grid polarizer (WP50H-Z, Thorlabs) at the front of the infrared camera.

Radiative Cooling Experiments. Regarding the radiative cooling experiment in the open system, an adhesive electric heater (HT24S, Thorlabs) was used. The temperature cycling was driven with modulation of voltages using a programmable power supply (2280S, Keithley). A cycle consisted of 6 min of heating and 2 min of cooling. The temporal variations in temperature were recorded on the bottom surface of the Si using adhesive thermocouples (SA1-K-72, Omega Engineering). The measurements were recorded at intervals of 10 s on a data logger (RDXL 12 SD, Omega Engineering). For the radiative cooling experiment in the closed configuration, we used a copper plate for the cover with the same setup as that for the open system. Here, we applied an input voltage of 15 V for 10 min.

ASSOCIATED CONTENT

Supporting Information

The Supporting Information is available free of charge at https://pubs.acs.org/doi/10.1021/acsnano.3c01184.

> Thermal emission characteristics of microcavities filled with various materials, AlO_X-based thermal emitters, SiC-based Berreman configuration, SEM images of the fabricated microcavities, energy-momentum dispersions of SiO_2/AlO_X (100/100 nm) and AlO_X/SiO_2 (100/100 nm) double shells, measured average emissivity values as a function of incident angle, angle-selective infrared camouflaging, statistical analysis with the surrogate model of Bayesian optimization, radiative cooling experiments in open and closed systems (PDF)

AUTHOR INFORMATION

Corresponding Authors

Run Hu − *School of Energy and Power Engineering, Huazhong University of Science and Technology, Wuhan 430074, China;* orcid.org/0000-0003-0274-9982; Email: hurun@hust.edu.cn

Eungkyu Lee − *Department of Electronic Engineering, Kyung Hee University, Gyeonggi-do 17104, Republic of Korea;* orcid.org/0000-0002-0211-0727; Email: eleest@khu.ac.kr

Sun-Kyung Kim − *Department of Applied Physics, Kyung Hee University, Gyeonggi-do 17104, Republic of Korea;* orcid.org/0000-0002-0715-0066; Email: sunkim@khu.ac.kr

Authors

Jin-Woo Cho − *Department of Applied Physics, Kyung Hee University, Gyeonggi-do 17104, Republic of Korea*

Yun-Jo Lee − *Department of Applied Physics, Kyung Hee University, Gyeonggi-do 17104, Republic of Korea*

Jae-Hyun Kim − *Department of Applied Physics, Kyung Hee University, Gyeonggi-do 17104, Republic of Korea*

Complete contact information is available at: https://pubs.acs.org/10.1021/acsnano.3c01184

Author Contributions

J.-W.C. and S.-K.K. conceived and designed the experiments. J.-W.C., Y.-J. L., and J.-H.K. measured the optical characteristics. J.-W.C performed the electromagnetic simulations. J.-W.C. and Y.-J.L. fabricated the structures. J.-W.C. and E.L. performed the Bayesian optimization method. R.H., E.L., and S.-K.K. supervised the project. All authors assisted in the analysis and interpretation of the data.

Notes

The authors declare no competing financial interest.

ACKNOWLEDGMENTS

S.-K.K. was supported by the National Research Foundation of Korea through the Nano Material Technology Development Program (2022M3H4A1A02046445) and the Basic Science Research Program (RS-2023-00207966) and the KIST institutional research program (2E32541).

REFERENCES

(1) Fan, S.; Li, W. Photonics and Thermodynamics Concepts in Radiative Cooling. *Nat. Photonics* **2022**, *16*, 182−190.
(2) Baranov, D. G.; Xiao, Y.; Nechepurenko, I. A.; Krasnok, A.; Alù, A.; Kats, M. A. Nanophotonic Engineering of Far-Field Thermal Emitters. *Nat. Mater.* **2019**, *18*, 920−930.
(3) Li, Y.; Li, W.; Han, T.; Zheng, X.; Li, J.; Li, B.; Fan, S.; Qiu, C. W. Transforming Heat Transfer with Thermal Metamaterials and Devices. *Nat. Rev. Mater.* **2021**, *6*, 488−507.
(4) Inoue, T.; Zoysa, M. De; Asano, T.; Noda, S. Realization of Dynamic Thermal Emission Control. *Nat. Mater.* **2014**, *13*, 928−931.
(5) Lenert, A.; Bierman, D. M.; Nam, Y.; Chan, W. R.; Celanović, I.; Soljačić, M.; Wang, E. N. A Nanophotonic Solar Thermophotovoltaic Device. *Nat. Nanotechnol.* **2014**, *9*, 126−130.
(6) Rinnerbauer, V.; Ndao, S.; Yeng, Y. X.; Chan, W. R.; Senkevich, J. J.; Joannopoulos, J. D.; Soljačić, M.; Celanovic, I. Recent Developments in High-Temperature Photonic Crystals for Energy Conversion. *Energy Environ. Sci.* **2012**, *5*, 8815−8823.
(7) Greffet, J. J.; Carminati, R.; Joulain, K.; Mulet, J. P.; Mainguy, S.; Chen, Y. Coherent Emission of Light by Thermal Sources. *Nature* **2002**, *416*, 61−64.
(8) Argyropoulos, C.; Le, K. Q.; Mattiucci, N.; D'Aguanno, G.; Alù, A. Broadband Absorbers and Selective Emitters Based on Plasmonic Brewster Metasurfaces. *Phys. Rev. B - Condens. Matter Mater. Phys.* **2013**, *87*, 205112.
(9) Lee, I. H.; Yoo, D.; Avouris, P.; Low, T.; Oh, S. H. Graphene Acoustic Plasmon Resonator for Ultrasensitive Infrared Spectroscopy. *Nat. Nanotechnol.* **2019**, *14*, 313−319.
(10) Cho, J.-W.; Park, S.-J.; Park, S.-J.; Kim, Y.-B.; Moon, Y.-J.; Kim, S.-K. Cooling Metals via Gap Plasmon Resonance. *Nano Lett.* **2021**, *21*, 3974−3980.
(11) Dyachenko, P. N.; Molesky, S.; Petrov, A. Y.; Störmer, M.; Krekeler, T.; Lang, S.; Ritter, M.; Jacob, Z.; Eich, M. Controlling Thermal Emission with Refractory Epsilon-near-Zero Metamaterials via Topological Transitions. *Nat. Commun.* **2016**, *7*, 11809.
(12) Raman, A. P.; Anoma, M. A.; Zhu, L.; Rephaeli, E.; Fan, S. Passive Radiative Cooling below Ambient Air Temperature under Direct Sunlight. *Nature* **2014**, *515*, 540−544.
(13) He, M.; Nolen, J. R.; Nordlander, J.; Cleri, A.; McIlwaine, N. S.; Tang, Y.; Lu, G.; Folland, T. G.; Landman, B. A.; Maria, J. P.; Caldwell, J. D. Deterministic Inverse Design of Tamm Plasmon Thermal Emitters with Multi-Resonant Control. *Nat. Mater.* **2021**, *20*, 1663−1669.
(14) Kim, M.; Lee, D.; Son, S.; Yang, Y.; Lee, H.; Rho, J. Visibly Transparent Radiative Cooler under Direct Sunlight. *Adv. Opt. Mater.* **2021**, *9*, 2002226.
(15) Cho, J.-W.; Lee, E.-J.; Kim, S.-K. Full-Color Solar-Heat-Resistant Films Based on Nanometer Optical Coatings. *Nano Lett.* **2022**, *22*, 380−388.
(16) Kim, S.; Shang, W.; Moon, S.; Pastega, T.; Lee, E.; Luo, T. High-Performance Transparent Radiative Cooler Designed by Quantum Computing. *ACS Energy Lett.* **2022**, *7*, 4134−4141.
(17) Xu, J.; Mandal, J.; Raman, A. P. Broadband Directional Control of Thermal Emission. *Science* **2021**, *372*, 393−397.
(18) Kim, S.; Zheng, C. Y.; Schatz, G. C.; Aydin, K.; Kim, K. H.; Mirkin, C. A. Mie-Resonant Three-Dimensional Metacrystals. *Nano Lett.* **2020**, *20*, 8096.
(19) Schuller, J. A.; Taubner, T.; Brongersma, M. L. Optical Antenna Thermal Emitters. *Nat. Photonics* **2009**, *3*, 658−661.
(20) Cho, J.-W.; Park, S.-J.; Park, S.-J.; Kim, Y.-B.; Kim, K. Y.; Bae, D.; Kim, S.-K. Scalable On-Chip Radiative Coolers for Concentrated Solar Energy Devices. *ACS Photonics* **2020**, *7*, 2748−2755.
(21) Tang, K.; Dong, K.; Li, J.; Gordon, M. P.; Reichertz, F. G.; Kim, H.; Rho, Y.; Wang, Q.; Lin, C. Y.; Grigoropoulos, C. P.; Javey, A.; Urban, J. J.; Yao, J.; Levinson, R.; Wu, J. Temperature-Adaptive Radiative Coating for All-Season Household Thermal Regulation. *Science* **2021**, *374*, 1504−1509.
(22) Kats, M. A.; Blanchard, R.; Zhang, S.; Genevet, P.; Ko, C.; Ramanathan, S.; Capasso, F. Vanadium Dioxide as a Natural Disordered Metamaterial: Perfect Thermal Emission and Large Broadband Negative Differential Thermal Emittance. *Phys. Rev. X* **2013**, *3*, 1−7.
(23) Kinsey, N.; DeVault, C.; Boltasseva, A.; Shalaev, V. M. Near-Zero-Index Materials for Photonics. *Nat. Rev. Mater.* **2019**, *4*, 742−760.
(24) Berreman, D. W. Infrared Absorption at Longitudinal Optic Frequency in Cubic Crystal Films. *Phys. Rev.* **1963**, *130*, 2193−2198.
(25) Vassant, S.; Hugonin, J.-P.; Marquier, F.; Greffet, J.-J. Berreman Mode and Epsilon near Zero Mode. *Opt. Express* **2012**, *20*, 23971.
(26) Harbecke, B.; Heinz, B.; Grosse, P. Optical Properties of Thin Films and the Berreman Effect. *Appl. Phys. A Solids Surfaces* **1985**, *38*, 263−267.
(27) Sakotic, Z.; Krasnok, A.; Cselyuszka, N.; Jankovic, N.; Alu, A. Berreman Embedded Eigenstates for Narrow-Band Absorption and Thermal Emission. *Phys. Rev. Appl.* **2020**, *13*, 064073.
(28) Heo, S. Y.; Lee, G. J.; Kim, D. H.; Kim, Y. J.; Ishii, S.; Kim, M. S.; Seok, T. J.; Lee, B. J.; Lee, H.; Song, Y. M. A Janus Emitter for Passive Heat Release from Enclosures. *Sci. Adv.* **2020**, *6*, 1−9.
(29) Cho, J.-W.; Yoon, S. S.; Lee, E.-J.; Kim, S.-K. Anti-Greenhouse Effect via Regulation of Surface Emissivity. *IEEE Photonics J.* **2022**, *14*, 1−7.
(30) Kitamura, R.; Pilon, L.; Jonasz, M. Optical Constants of Silica Glass from Extreme Ultraviolet to Far Infrared at near Room Temperature. *Appl. Opt.* **2007**, *46*, 8118−8133.
(31) Shaykhutdinov, T.; Furchner, A.; Rappich, J.; Hinrichs, K. Mid-Infrared Nanospectroscopy of Berreman Mode and Epsilon-near-Zero Local Field Confinement in Thin Films. *Opt. Mater. Express* **2017**, *7*, 3706.
(32) Kischkat, J.; Peters, S.; Gruska, B.; Semtsiv, M.; Chashnikova, M.; Klinkmüller, M.; Fedosenko, O.; MacHulik, S.; Aleksandrova, A.; Monastyrskyi, G.; Flores, Y.; Masselink, W. T. Mid-Infrared Optical Properties of Thin Films of Aluminum Oxide, Titanium Dioxide, Silicon Dioxide, Aluminum Nitride, and Silicon Nitride. *Appl. Opt.* **2012**, *51*, 6789−6798.
(33) Kim, Y.-B.; Cho, J.-W.; Lee, Y.-J.; Bae, D.; Kim, S.-K. High-Index-Contrast Photonic Structures: A Versatile Platform for Photon Manipulation. *Light: Sci. Appl.* **2022**, *11*, 316.
(34) Shahriari, B.; Swersky, K.; Wang, Z.; Adams, R. P.; De Freitas, N. Taking the Human out of the Loop: A Review of Bayesian Optimization. *Proc. IEEE* **2016**, *104*, 148−175.
(35) Cai, L.; Peng, Y.; Xu, J.; Zhou, C. C. C.; Zhou, C. C. C.; Wu, P.; Lin, D.; Fan, S.; Cui, Y. Temperature Regulation in Colored Infrared-Transparent Polyethylene Textiles. *Joule* **2019**, *3*, 1478−1486.
(36) Hastings, S.; Kim, S. W.; Brown, R. D. Face Temperature as an Indicator of Thermal Stress in Outdoor Work Environments. *Atmospher* **2020**, *11*, 627.
(37) Wang, Z.; He, R.; Chen, K. Thermal Comfort and Virtual Reality Headsets. *Appl. Ergon.* **2020**, *85*, 103066.
(38) Cengel, Y. A.; Ghajar, A. J. *Heat and Mass Transfer: Fundametals and Applications*, 5th ed; McGraw-Hill Education: New York, 2014.
(39) Anopchenko, A.; Tao, L.; Arndt, C.; Lee, H. W. H. Field-Effect Tunable and Broadband Epsilon-Near-Zero Perfect Absorbers with Deep Subwavelength Thickness. *ACS Photonics* **2018**, *5*, 2631−2637.
(40) Kim, J.-H.; Cho, J.-W.; Jeon, I.; Jeong, K. T.; Kang, H.-J.; Choi, D.-G.; Kim, J. H.; Kim, S. K. Synergistically designed antireflective cover for improving wide-angle photovoltaic efficiencies. *Opt. Exp.* **2022**, *30*, 42406−42414.
(41) Krayer, L. J.; Kim, J.; Garrett, J. L.; Munday, J. N. Optoelectronic Devices on Index-near-Zero Substrates. *ACS Photonics* **2019**, *6*, 2238−2244.
(42) Alam, M. Z.; De Leon, I.; Boyd, R. W. Large Optical Nonlinearity of Indium Tin Oxide in Its Epsilon-near-Zero Region. *Science* **2016**, *352*, 795−797.
(43) Pedregosa, F.; Varoquax, G.; Gramfort, A.; Michel, V.; Thirion, B.; Grisel, O.; Blondel, M.; Prettenhofer, P.; Welss, R.; Dubourg, V.; Vanderplas, J.; Passos, A.; Cournapeau, D.; Brucher, M.; Perrot, M.;

https://doi.org/10.1021/acsnano.3c01184
ACS Nano 2023, 17, 10442−10451

Duchesnay, E. Scikit-learn: Machine Learning in Python. *J. Mach. Learn. Res.* **2011**, *12*, 2825−2830.
(44) Rasmussen, C. E.; Williams, C. K. I. *Gaussian Processes for Machine Learning*; The MIT Press: Cambridge, 2006.

https://doi.org/10.1021/acsnano.3c01184
ACS Nano 2023, 17, 10442−10451